Supporting Information

Structurally Self-Anchored Bipolar Membranes with Interlocked Interfaces for Coupled Hydrogen Production and Biomass Electrosynthesis

Sihan Li [a,c], Jiaojiao Jiang [a,b], Miaomiao Wu[c,], Chunxiao Wu [a,b,]*, Chao Yang [a,b]*

[a] State Key Laboratory of Biopharmaceutical Preparation and Delivery, Institute of Process Engineering, Chinese Academy of Sciences, Beijing 100190, China

[b] School of Chemical Engineering, University of Chinese Academy of Sciences, Beijing 100049, China

[c] School of Chemical and Environmental Engineering, China University of Mining and Technology (Beijing), Beijing 100083, China

* To whom correspondence should be addressed: E-mail: cxwu@ipe.ac.cn

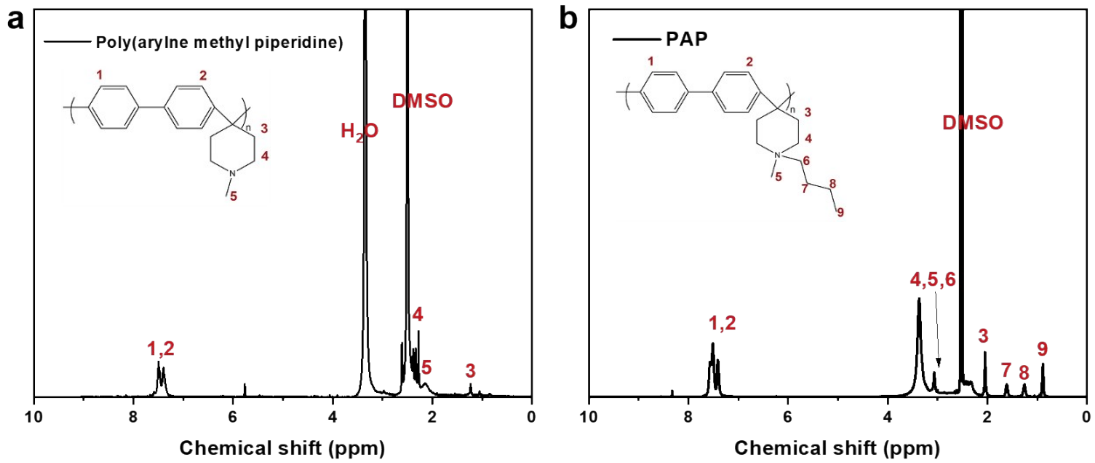

Fig. S1 ^{1}H NMR spectra of a) poly (arylene methyl piperidine) and b) PAP.

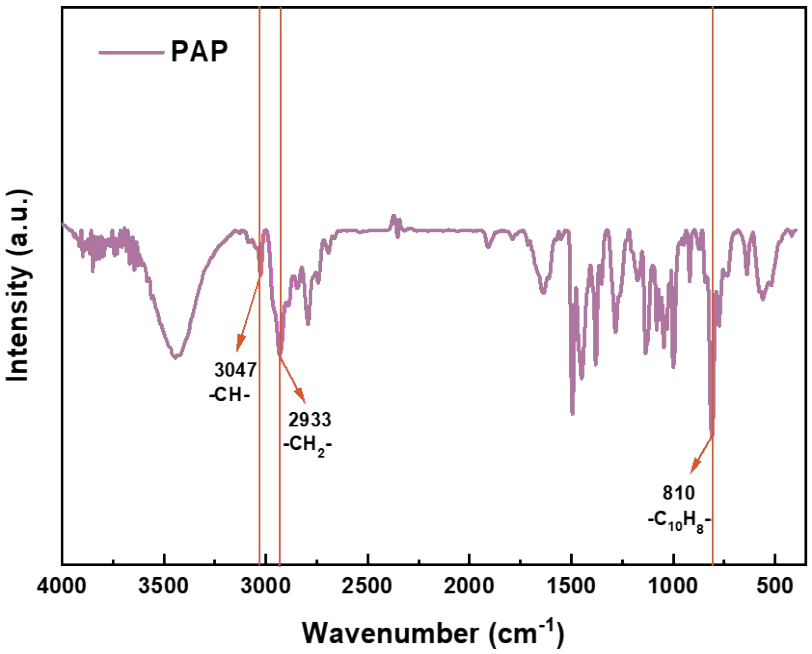

Fig. S2 FTIR image of PAP.

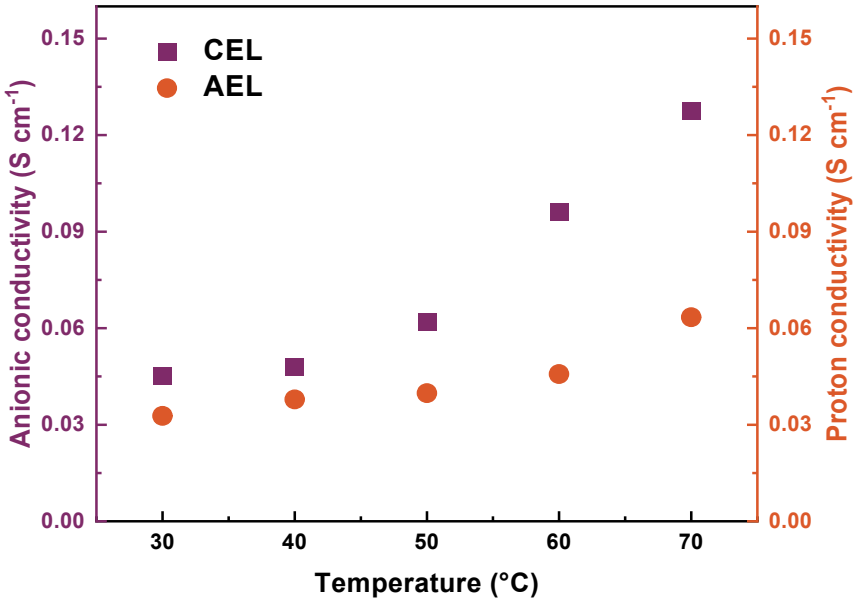

Fig. S3 Anionic conductivity of AEM and proton conductivity of PEM at different temperature.

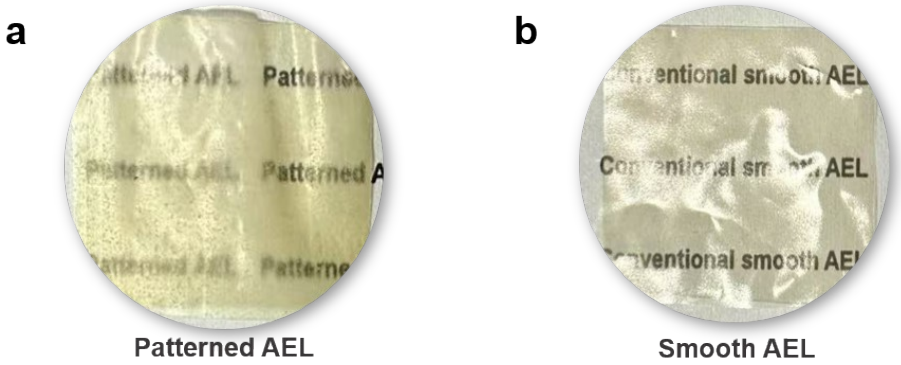

Fig. S4 Digital photographs of the anion exchange layer, a) patterned AEL, b) smooth surface AEL

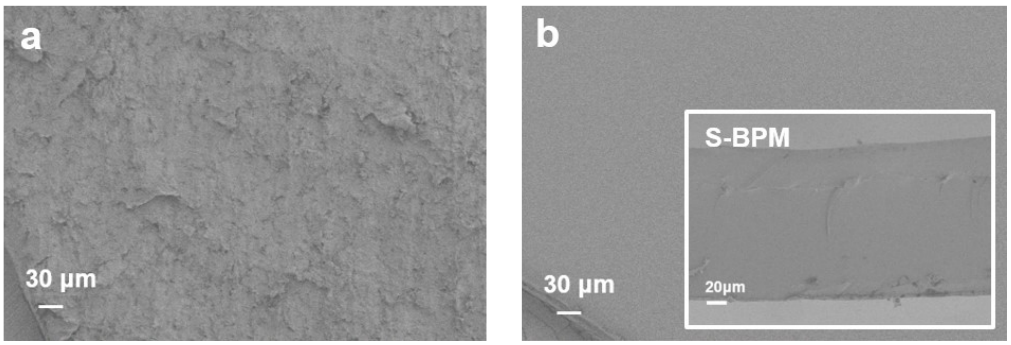

Fig. S5 SEM image of a) patterned AEL, b) smooth surface AEL. Inset of b) shows the cross-sectional SEM image of S-BPM.

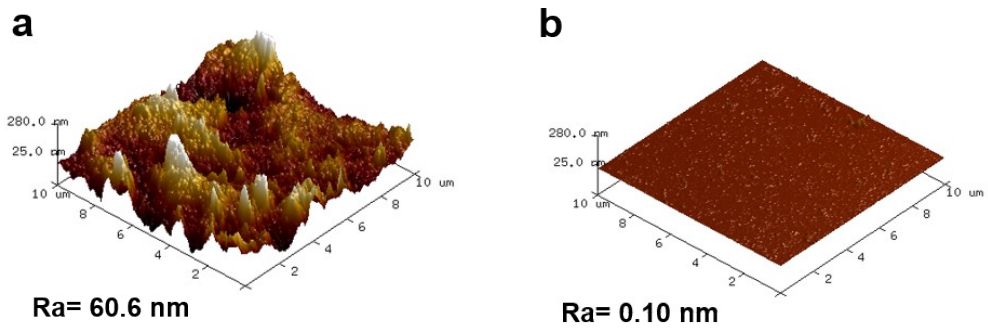

Fig. S6 Representative AFM topography comparison of membrane surface roughness: a) patterned AEL, b) smooth surface AEL.

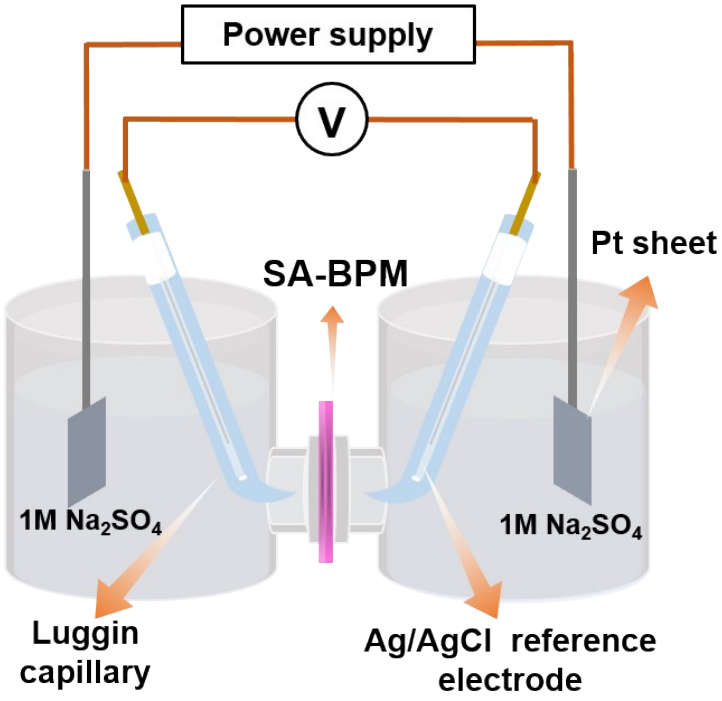

Figure S7. Schematic illustration of 4-electrode cell used to evaluate BPM polarization behavior.

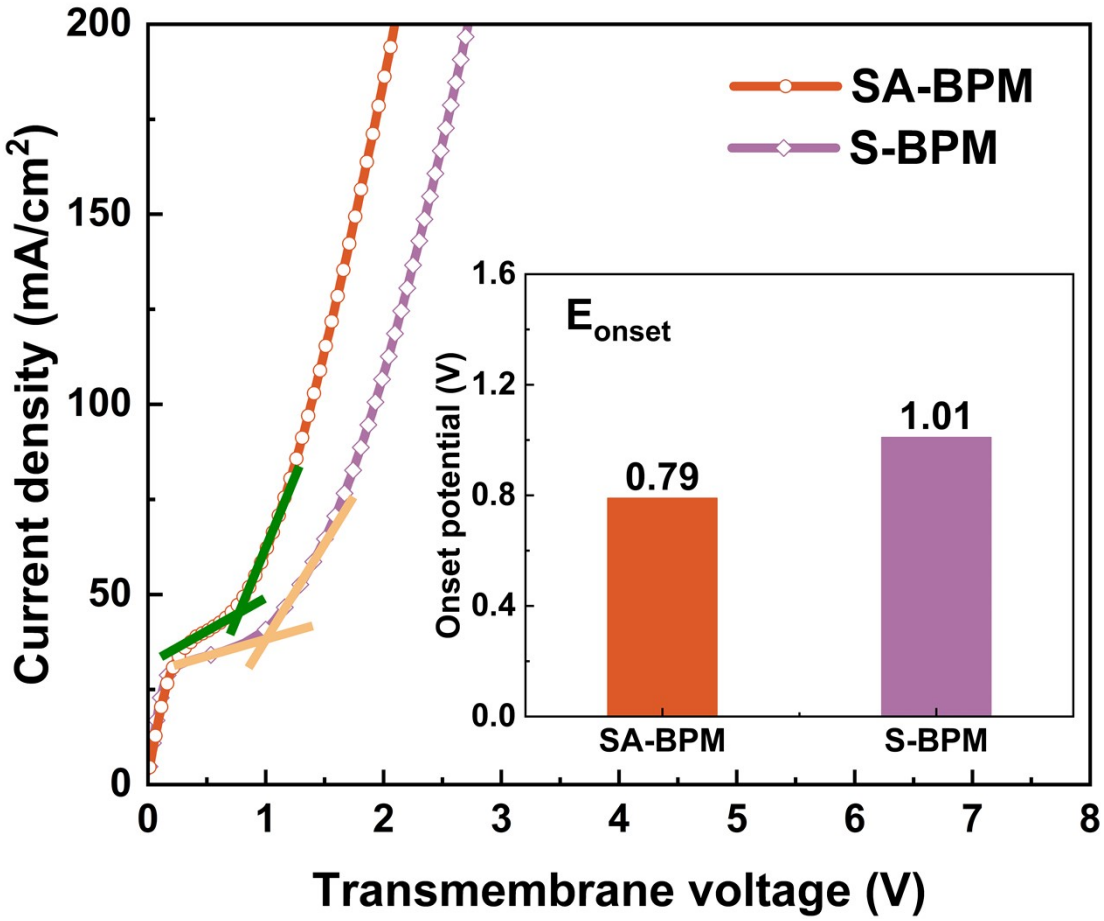

Fig. S8 Onset potential determination of SA-BPM, and S-BPM.

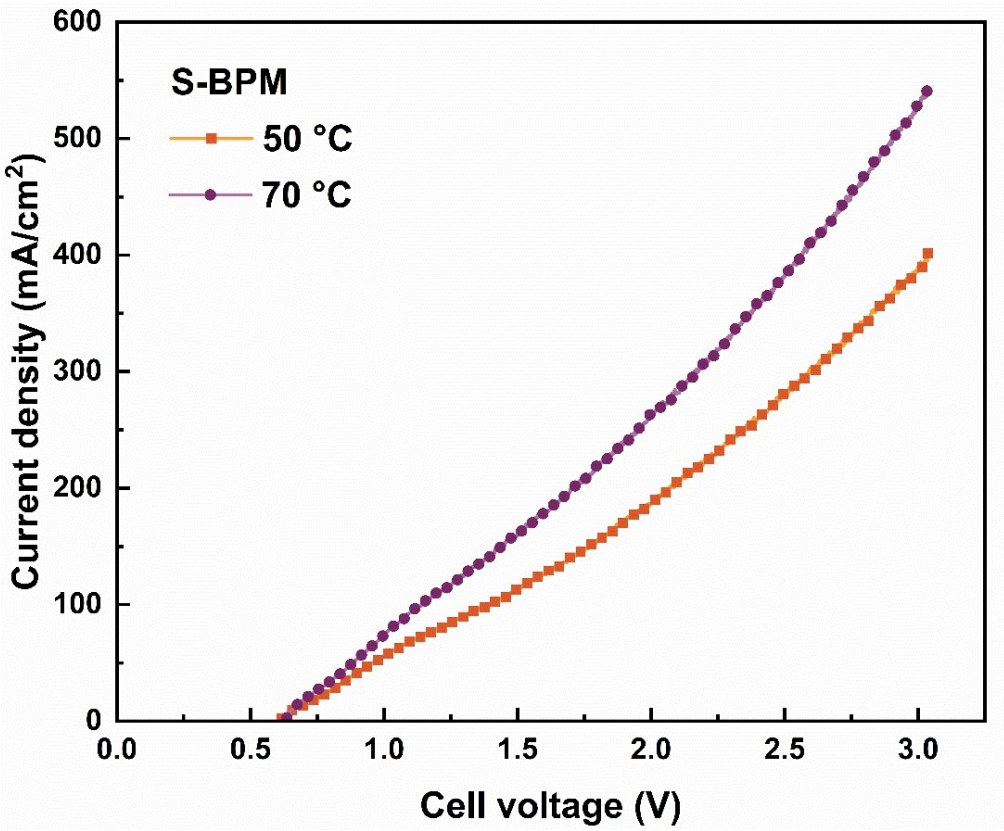

Fig. S9 I-V curves of S-BPM at 50℃ and 70℃.

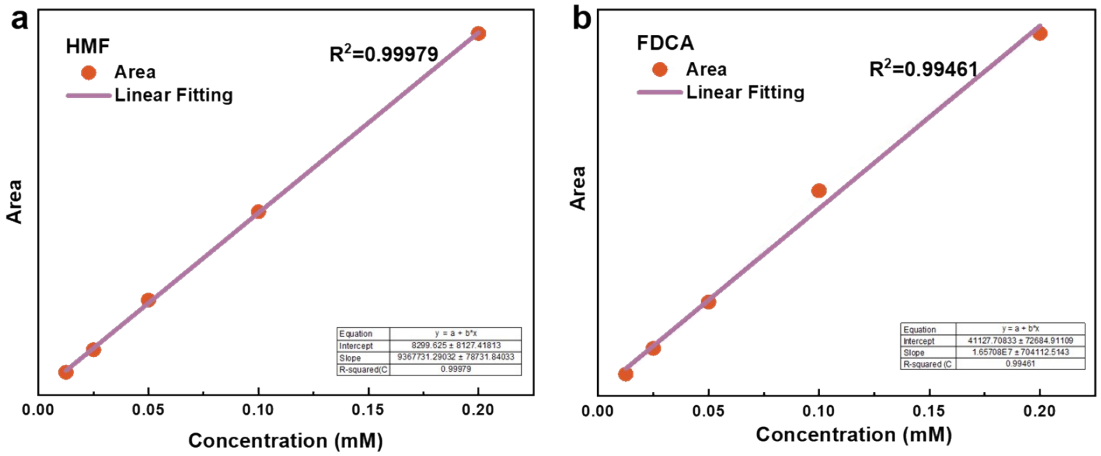

Fig. S10 a) The standard curve of HMF by plotting the HMF concentration with respect to the absolute HPLC peak area. b) The standard curve of FDCA by plotting the FDCA concentration with respect to the absolute HPLC peak area.

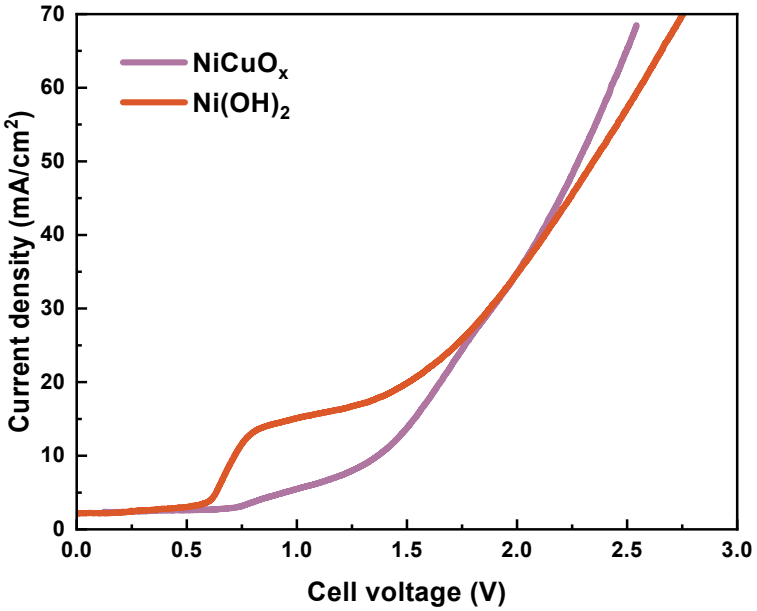

Fig. S11 I-V curves using different HMFOR catalytic electrodes.

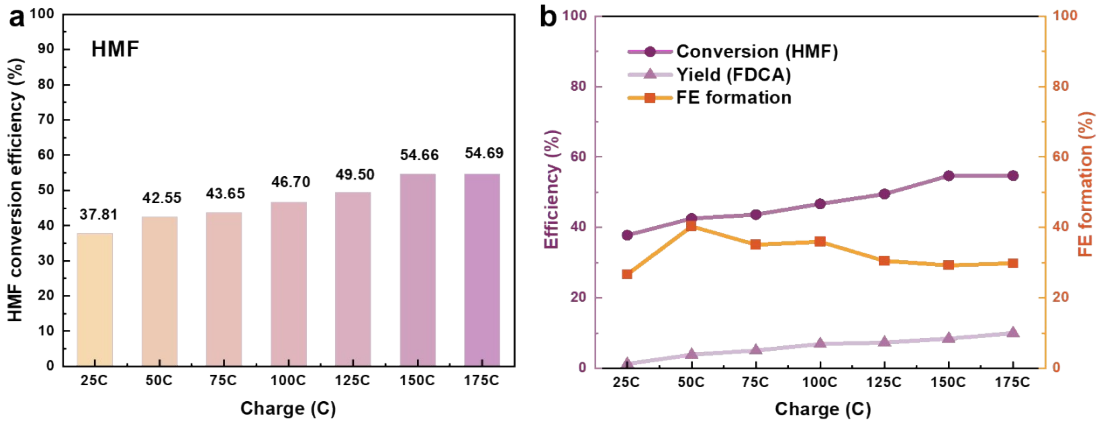

Fig. S12 Performance of HER coupling HMFOR with $Ni(OH)_2$ as anode. a) HMF conversion efficiency; b) HMF conversion, FDCA yield, and FE formation in the electrolyzer.

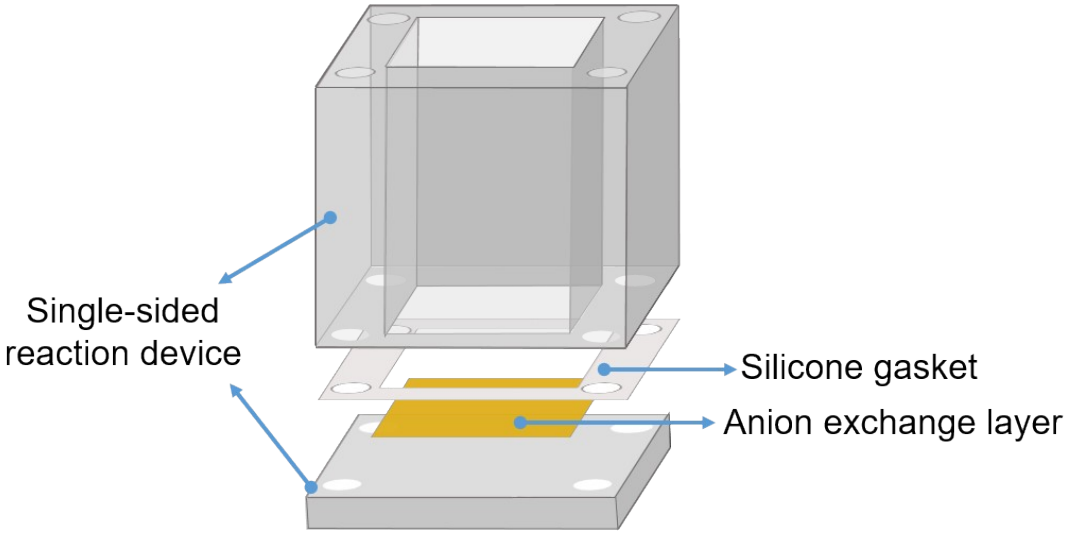

Fig. S13 Schematic illustration of the membrane single-sided reaction device used for preparing the catalyst layer.

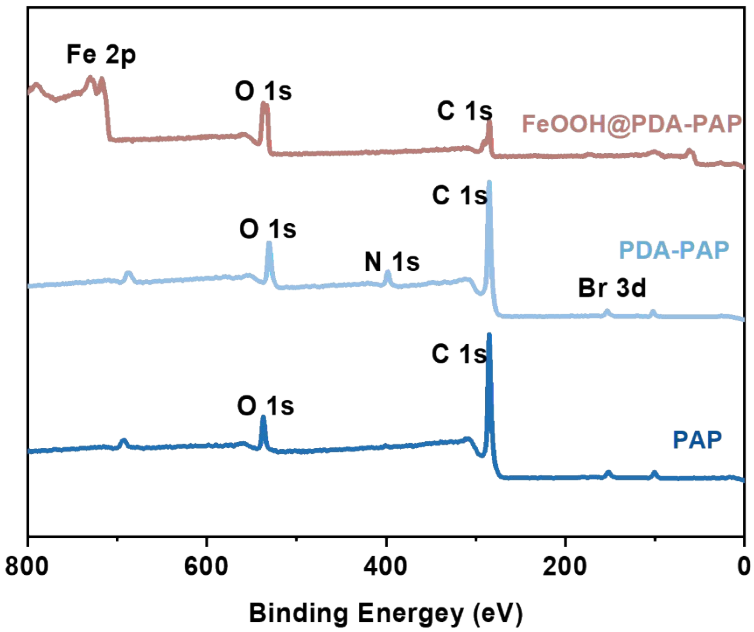

Fig. S14 XPS survey spectra of PAP, PDA–PAP, and FeOOH@PDA–PAP. For PAP and PDA–PAP, characteristic signals of C 1s, O 1s, N 1s, and Br 2d are observed. Compared with PAP, PDA–PAP shows a markedly increased N 1s intensity, consistent with the successful introduction of the PDA layer. After FeOOH deposition, FeOOH@PDA–PAP exhibits the appearance of Fe-related signals, while the N 1s signal becomes attenuated, which is consistent with partial surface coverage of the underlying PDA–PAP by the FeOOH overlayer (attenuation of the photoelectron signal through the overlayer), supporting the successful construction of the FeOOH@PDA catalytic layer.

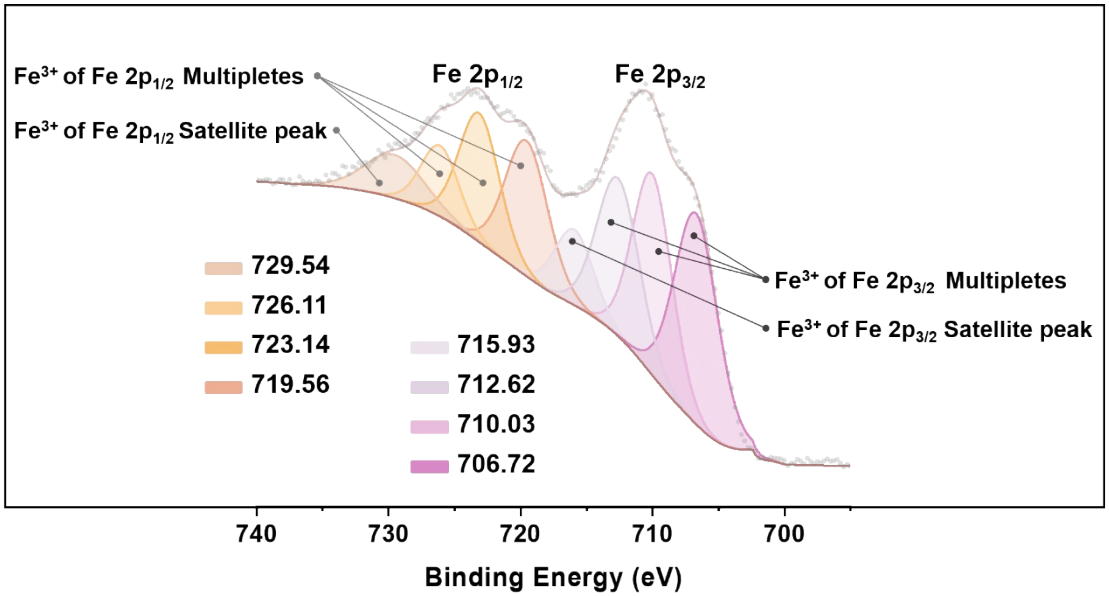

Fig. S15 High-resolution XPS Fe 2p spectrum of FeOOH@PDA–PAP. The Fe 2p region (typically ~700–740 eV) shows the Fe $2p_{3/2}$ and Fe $2p_{1/2}$ components accompanied by characteristic satellite features. Peak deconvolution of the Fe 2p envelope yields multiple components associated with Fe(III) species, which is consistent with the formation of an Fe(III) oxyhydroxide (FeOOH-like) overlayer on PDA–PAP.

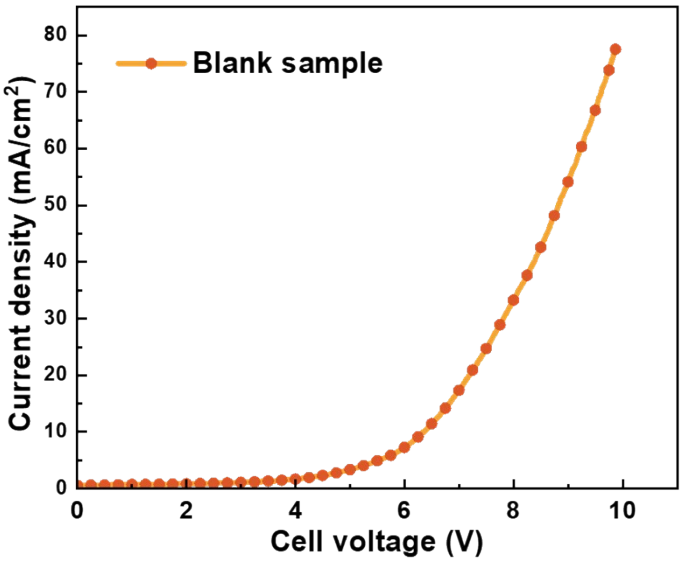

Fig. S16 The I–V curve of blank sample (catalyst-free SA-BPM) at 30 °C.

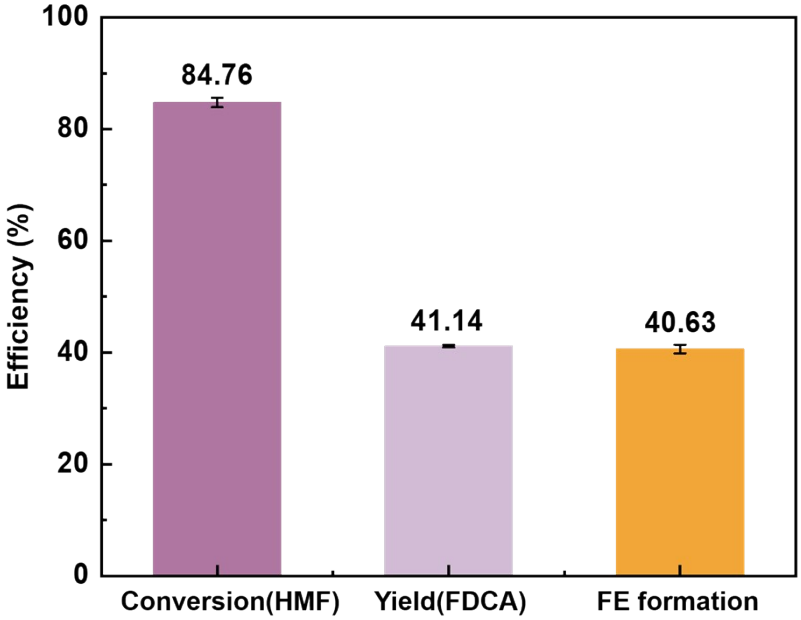

Fig. S17 Mean values and standard deviations of HMF conversion, FDCA yield, and FE for HMFOR coupled with HER of three independent measurements.

Table S1. IEC of Anion exchange layer (PAP) and cation exchange layer (PFSA).

Samples	IEC (meg g^{-1})
AEL	2.315
CEL	1.139